Exp Fluids (2016) 57:80
DOI 10.1007/s00348-016-2158-0

RESEARCH ARTICLE

Tomographic PIV behind a prosthetic heart valve

D. Hasler[1] · A. Landolt[2] · D. Obrist[1]

Received: 3 December 2015 / Revised: 4 March 2016 / Accepted: 4 April 2016

Abstract The instantaneous three-dimensional velocity field past a bioprosthetic heart valve was measured using tomographic particle image velocimetry. Two digital cameras were used together with a mirror setup to record PIV images from four different angles. Measurements were conducted in a transparent silicone phantom with a simplified geometry of the aortic root. The refraction indices of the silicone phantom and the working fluid were matched to minimize optical distortion from the flow field to the cameras. The silicone phantom of the aorta was integrated in a flow loop driven by a piston pump. Measurements were conducted for steady and pulsatile flow conditions. Results of the instantaneous, ensemble and phase-averaged flow field are presented. The three-dimensional velocity field reveals a flow topology, which can be related to features of the aortic valve prosthesis.

1 Introduction

Tomographic particle image velocimetry (tomo-PIV) is a powerful tool in experimental fluid dynamics for measuring all three velocity components in three-dimensional flow domains (3D3C). Since its introduction (Elsinga et al. 2005, 2006), tomo-PIV has been applied to a variety of flows e.g., free shear flows [circular jets (Violato and Scarano 2011), wakes (Scarano and Poelma 2009)] and boundary layer flow (Atkinson et al. 2010). Recently a number of time-resolved tomo-PIV measurements of unsteady flows have been conducted using high speed cameras (Elsinga and Marusic 2010; Schröder et al. 2008, 2011). It was shown that the obtained spatio-temporal data can be used to identify dynamic modes of the flow field (Schmid et al. 2012). The first application of tomo-PIV to internal flows in complex geometries is due to Buchmann et al. (2011) who studied the flow in the human carotid artery, comparing stereoscopic to tomographic PIV results under steady flow conditions. Buchmann et al. (2011) reported bias errors due to ghost particles in tomo-PIV measurements and discrepancies in the RMS error between stereo and tomo-PIV in certain regions of elevated velocity gradients of up to 10 %. Furthermore, RMS errors where found to be higher for thicker light sheets used in the tomo-PIV measurements. Overall a good agreement between the stereo PIV and the tomo-PIV results was found with RMS errors varying in the range of 0.1–0.3 pixels. A detailed presentation of tomographic PIV, its background and a wide range of applications is given in the topical review paper by Scarano (2012).

This study presents the first tomo-PIV measurement of the flow past a bioprosthetic heart valve. In contrast to so-called mechanical heart valves (e.g., made of titanium and pyrolytic carbon), bioprosthetic valves are fabricated from biological tissue (e.g., bovine pericardium). Prostheses are used to replace diseased native heart valves (e.g., stenotic or insufficient valves) most often in aortic position.

The design of bioprosthetic heart valves is motivated by the anatomy of native aortic heart valves with three cusps. It is believed that this biomimetic design leads to blood flow which is similar to the physiological flow

Electronic supplementary material The online version of this article (doi:10.1007/s00348-016-2158-0) contains supplementary material, which is available to authorized users.

✉ D. Hasler
david.hasler@artorg.unibe.ch

[1] ARTORG Center for Biomedical Engineering Research, University of Bern, Bern, Switzerland

[2] streamwise GmbH, Männedorf, Switzerland

Published online: 03 May 2016

in native valves. This helps to mitigate a major drawback of mechanical valves: blood trauma caused by non-physiological blood flow requiring life-long anticoagulant therapy. At the same time, bioprostheses are known to suffer from structural valve deterioration leading to mechanical defects and requiring replacement of the prosthesis after 10–20 years (Jamieson et al. 2001), whereas mechanical valves are known to last a lifetime. This leads to a classical engineering problem: How to design heart valve prostheses which combine the benefits of bioprostheses (no blood trauma) with the high durability of mechanical valves? To this end, it is important to obtain a detailed understanding of the fluid mechanics of heart valves because specific flow features (e.g., excessive shear stress, flow separation, stagnation regions, vortical flow) are important factors for the overall valve performance.

Mechanical heart valves have only few kinematic degrees of freedom (typically only one or two tilting disks) and high levels of symmetry due to their man-made design. This enabled a number of experimental studies with classical two-dimensional PIV (e.g., Bellofiore and Quinlan 2011; Manning et al. 2003; Brücker et al. 2002; Dasi et al. 2007; Ge et al. 2005) and stereoscopic PIV (Kaminsky et al. 2007) as well as defocusing digital PIV (Amatya et al. 2009). In a recent conference contribution, Hegner et al. (2015) presented results of tomographic PIV and 3D particle tracking velocimetry (PTV) of the flow past a trileaflet mechanical valve. Numerical studies with computational models of mechanical heart valves have been conducted by Tullio et al. (2009), Borazjani et al. (2010), Ge et al. (2003) and Dasi et al. (2007).

Bioprosthetic valves have a more complex geometry due to the three-cusp design. Their dynamics is governed by the tight interaction between the flow and the soft cusp tissue leading to fluttering and vortex shedding. Therefore, the resulting flow field is more complex than in mechanical heart valves and it is difficult to obtain a good understanding of the flow by two-dimensional measurements alone. Leo et al. (2006) used stereoscopic PIV (2D3C) to study the out-of-plane flow of a (polymeric) prosthesis with three cusps. Scanning through different planes of the region of interest yielded a three-dimensional representation of the flow. Computational models have been proposed, for instance, by Griffith (2012) and Borazjani (2013) providing numerical predictions for the three-dimensional unsteady flow field past prototypical valves with three cusps. Finally, 4D phase-contrast magnetic resonance imaging (4D-PC-MRI) has been used to measure the flow past native aortic valves in vivo (Markl et al. 2007, 2011). However, this method suffers from long acquisition times and limited resolution.

Fig. 1 Surgical aortic valve bioprosthesis (*Carpentier–Edwards Aortic Model 2625*) used in experiments

It is the objective of this work to introduce an experimental setup for the study of the three-dimensional unsteady flow field past heart valves using tomo-PIV. The presented results shall serve as a typical example for the flow past bioprosthetic valves to illustrate the basic structure of such flow fields and to demonstrate the capabilities of the proposed experimental setup. It is not the aim of this paper to relate specific features of the measured flow field to the clinical performance of this valve.

Results are presented for a *Carpentier–Edwards 2625* valve (Edwards Lifescience Inc., Irvine, USA) made from porcine pericardium (Fig. 1). The design of this valve is very typical for bioprosthetic valves such that our results can serve as a baseline for the discussion of the three-dimensional flow field past bioprosthetic heart valves.

2 Methods

The setup for the tomo-PIV experiment (Fig. 2) for measuring the flow field past bioprosthetic valves consists of several elements: the test cell (1) holds the bioprosthetic valve which is firmly inserted in a transparent silicone model (phantom) of the aortic root. This test cell is integrated in a pulsatile flow loop which is driven by a computer-controlled piston pump. The flow loop is filled with a water–glycerol mixture which is refraction index matched with the silicone model. Small neutrally buoyant fluorescent particles were added to the fluid. Upon illumination of the test cell with a laser (4), these particles emit light at a slightly higher wave length which is captured from different angles by CCD cameras (6). The system was synchronized using the phase of the piston pump as trigger signal. The two-dimensional particle images were combined by tomographic algorithms to reconstruct a three-dimensional representation of the particle cloud. Particle image cross-correlation was then applied to two particle clouds subsequently captured within a short time interval. This yielded three-dimensional velocity fields.

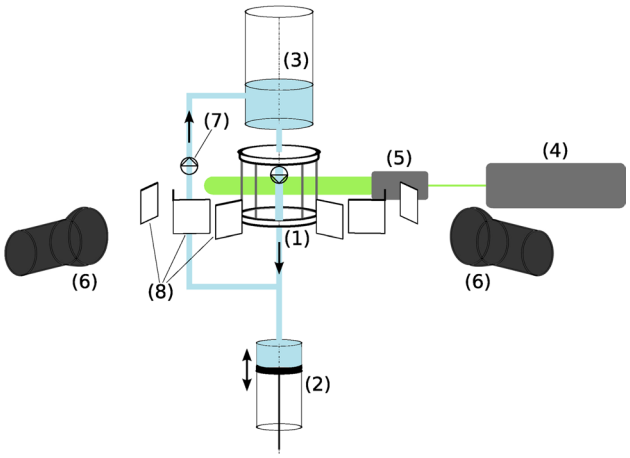

Fig. 2 Schematics of the experimental setup: test cell containing a silicone phantom of the aorta and the valve prosthesis (*1*); piston pump (*2*); tank (*3*); Nd:YAG laser (*4*); beam expander (*5*); CCD cameras (*6*) with mirrors (*8*) and a unidirectional valve in the feedback tube (*7*)

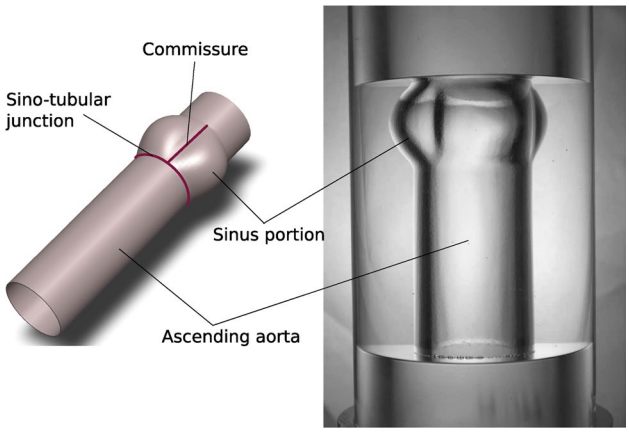

Fig. 3 3D model of the simplified aortic root after Swanson and Clark (1974) (*left*) used to fabricate a thick-walled silicone phantom (*right*)

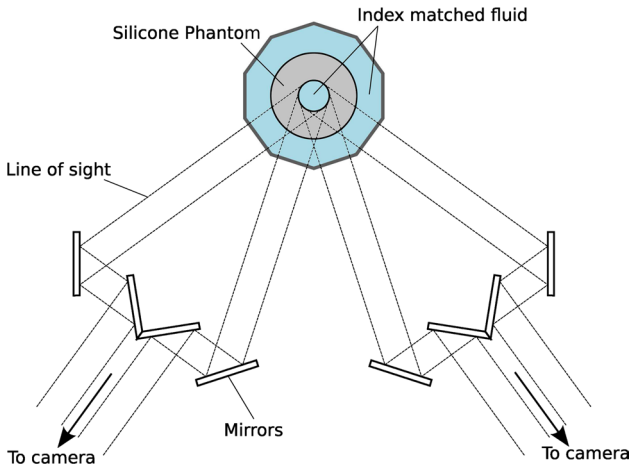

Fig. 4 Schematics of the top view of the test cell with mirror configuration for dual-view modality

We used two experimental protocols, one for constant and another for pulsatile flow: in the constant-flow protocol, multiple measurements were averaged to obtain a mean flow field. In the pulsatile flow measurement, the pump created a pulse velocity profile such that the tested valve opened and closed periodically.

In the following sections, the different elements of the experimental setup are described in more detail.

2.1 Physiological flow model

All measurements were done with a *Carpentier Edwards Model 2625 Aortic* valve (Edwards Lifesciences, Irvine, USA) with a nominal inner diameter of 23 mm.

The valve was inserted into a model of the aortic root consisting of the *sinus of Valsalva* (also, *sinus portion*) and a short section of the ascending aorta. To approximate the geometry of the aortic root, a parametrized geometry for the sinus portion (Swanson and Clark 1974) was combined with a straight tube with an inner diameter of 24 mm.

The material which is used to model the aortic root is optically transparent for the purpose of image recording and illumination. In particular for tomo-PIV measurements, the optical distortion between the measurement volume and the cameras has to be very small. Therefore, a negative mold of the aortic root geometry was 3D-printed with a rapid prototyping process and subsequently polished and painted to improve surface quality. This print was then used to cast a silicone phantom of the aortic root (Fig. 3). The used silicone (ELASTOSIL 601, Wacker Silicones, Germany) has very good transparency properties and a refraction index of 1.40–1.41. In addition, it can be poured which offers great flexibility in fabricating complex geometries (Geoghegan et al. 2012; Yousif et al. 2010).

The outside of this phantom was cylindrical with a diameter of 70 mm. This yielded a thick-walled structure such that the elastic deformations of the phantom during a pulse cycle remained negligibly small.

2.1.1 Test cell

The aortic root model was integrated in a transparent test cell composed of a 10-edge polygonal housing made of acrylic glass with an angle of 36° between the surface normals of two neighboring windows. It allowed virtually

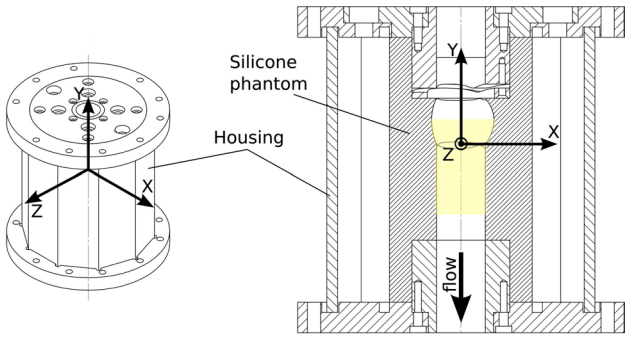

Fig. 5 Technical drawing of the cell (3D view *left*, sectional view *right*) with the ten-edge polygonal housing for the silicone. *Yellow shading* indicates measurement volume

undistorted optical access to the domain of interest from different angles. Four windows next to each other were used for four camera views which yielded a linear imaging configuration shown in Fig. 4 with a total aperture angle of 108° [see Scarano (2012) for more information about the imaging configuration].

The cell was closed by top and bottom lids made of anodized aluminum containing plugs for a tight connection with the silicone phantom. This ensured precise alignment between the silicone phantom and the central axis of the cell which was necessary for merging PIV results with the geometry of the phantom (see Sect. 2.2). Furthermore, the test cell featured a modular system for mounting heart valve prostheses. A technical drawing of the cell is shown in Fig. 5.

2.1.2 Flow loop

The physiological flow through the aortic heart valve and in the aortic root was modeled by a flow loop. The computer-controlled piston pump was connected to the bottom of the test cell (position (1) in Fig. 2). The reservoir (3) was connected to the pump by a feedback tube which contained a unidirectional valve (7) to ensure a circulating flow through the loop. During the descending motion of the piston pump (systolic phase), fluid flowed from the reservoir through the test cell. The mean flow velocity was adjusted by controlling the piston velocity. During the ascending motion of the pump (diastolic phase), fluid was fed back to the reservoir through the feedback tube.

The present version of the setup did not account for the physiological compliance of the systemic circulation. This allowed a better control of the flow in the test cell by means of the pump. For studies with a more physiological focus, a compliance chamber can be added to the flow loop as well as a resistor representing the total peripheral resistance of the systemic circulation (Stergiopulos et al. 1999).

2.1.3 Test fluid

To match the refraction index of the silicone phantom, a water–glycerol mixture (39/61, by weight) was used. The density of the water–glycerol mixture was $\rho = 1140$ kg/m^3 and its dynamic viscosity was 0.009 Pa s. This yielded a kinematic viscosity $\nu = \mu/\rho \approx 7.9 \times 10^{-6}$ m^2/s. Although this is approximately two times higher than in real blood, this fluid mixture was used because of the relatively easy handling. For experiments with a stronger focus on biomedical questions, this fluid can be replaced by other mixtures: Blake et al. (2009) used a water–glycerol–sodium chloride mixture to match the refraction index of silicone and approximate the kinematic viscosity of blood. Yousif et al. (2010) presented a method of producing a blood-mimicking fluid on the basis of water, glycerol and sodium iodide, which matches the refraction index for silicone as well as the kinematic viscosity of blood. However, this mixture can impair the optical quality of the PMMA housing after a certain time of exposure to the sodium iodide.

The test fluid filled the whole flow loop including the free space between the polygon housing of the test cell and the cylindrical silicone phantom (gap width ≈25 mm). The temperature of the test fluid was monitored before and after the measurement and remained within 4 % of the room temperature of 22 °C.

2.2 Tomographic PIV system

For the actual flow measurements, we used the FlowMaster Tomographic PIV system (LaVision, Göttingen, Germany). For all computational tasks described in the following, we used the software package DaVis (LaVision, Göttingen, Germany).

2.2.1 Camera configuration

A two camera system was used together with a mirror configuration to record simultaneous images from four different angles through four neighboring windows of the polygonal test cell. The lines of sight through the left and right pairs of neighboring windows were reflected with multiple mirrors (see Fig. 4) onto parallel lines of sight. The cameras were aligned with the respective bisectrix of the neighboring window pairs such that each camera recorded two different views on the left and right halves of the camera sensor. This composite camera image was subsequently treated as two images from separate cameras.

With this dual-view modality, effectively four images from different angles were recorded with only two cameras. The mirrors had to be mounted precisely and oriented carefully with respect to the cell housing in order to prevent optical interferences on the camera sensor. We used

two 8M 12 bit CCD Digital Camera (Imager LX, LaVision, Göttingen, Germany) with an aspect ratio of 4:3 and prime lenses with a focal length of $f = 100$ mm and a maximum aperture of $F2.8$ (Kenko Tokina, Tokyo, Japan). With the dual-view modality, each of the four recorded image had a resolution of 1656×2488 pixels and the maximum frame rate was 3.1 Hz which limited the possibilities for time-resolved measurements.

2.2.2 Illumination

For volume illumination, a double-pulse Nd:YAG laser (Nano L PIV, Litron Lasers, Rugby, England) emitting at 532 nm with a power of 235 mJ/pulse was used together with volume optics [Fig. 2(5)]. The direction of illumination was along the X-axis. The depth of the illumination volume was bigger than the maximum inner diameter of the phantom, >34 mm.

2.2.3 Particles

The test fluid was seeded with particles with diameters in the range of $d_P = 20 \ldots 50$ µm and a density of $\rho_P = 1180$ kg/m^3. The response time constant of these particles can be estimated as $\tau = \rho_p d_p^2/(18\mu) \approx 18$ µs (Raffel et al. 2007) indicating that the particle velocity follows very closely the local fluid velocity. A seeding density of 500–800 particles/cm^3 was used, which corresponded to a particle image density of 0.1–0.15 particles per pixel (ppp). The numerous interfaces and surfaces in the test cell and the relatively strong illumination can lead to significant reflections of the laser light which may interfere with the light scattered from the particles. To overcome this difficulty, spherical PMMA micro-particles with a fluorescent Rhodamine-B coating (Microparticles GmbH, Berlin, Germany) were used. The light emitted by the fluorescent coating was shifted toward longer wave lengths (584 nm) such that the unwanted reflections were effectively reduced by using a low-pass filter (570 nm cut-off) in front of the cameras.

2.2.4 Camera calibration

Tomographic PIV measurements require accurate mapping of the coordinates $[X, Y, Z]^T$ in the world reference frame to two-dimensional camera coordinates $[x, y]^T$. Generally, a mapping error of <0.4 pixels is needed throughout the measurement volume (Elsinga et al. 2006) for a successful tomographic reconstruction of the particle cloud.

The test cell offered the possibility of replacing the silicone phantom with a calibration plate which could be aligned with the symmetry axis of the cell. We used a calibration plate with precisely distributed marks on two levels of different depths (1 mm, apart) on the plate (LaVision, Göttingen, Germany). After mounting of the calibration plate, the whole cell was filled with the index-matched fluid to establish similar optical conditions as for the measurement with the silicone phantom. After calibration, the fluid was drained, the silicone phantom was inserted and the cell was closed with the top lid containing the prosthetic valve. The test cell (including the gap between the polygonal housing and the phantom) was then again filled with the index-matched fluid and re-connected to the flow loop.

For each of the four viewing angles, a third-order polynomial was fitted to image data of the calibration plate (Raffel et al. 2007). This function maps positions in the three-dimensional world coordinate frame $\{X, Y, Z\}$ to the positions on the two-dimensional camera sensor reference frame $\{x_i, y_i\}$, where $i = 1, 2, 3, 4$ for each of the four camera views. After replacing the calibration plate with the silicone phantom, this mapping of 3D world positions to 2D camera positions still suffered from differences between the refraction indices of the fluid and the silicone phantom, small optical impurities in the phantom, as well as from the remaining error after initial calibration. Volume self-calibration (Wieneke 2008) was applied to further reduce errors. To this end, images with a small seeding density (70 particles/cm^3 corresponding to approximately 0.035 ppp) were recorded under pulsatile flow conditions with a maximum mean velocity $\bar{u}_{max} = 0.1$ m/s [Fig. 6, see also Eq. (2) in Sect. 3.2] such that images of corresponding particles could be reliably identified on the different camera

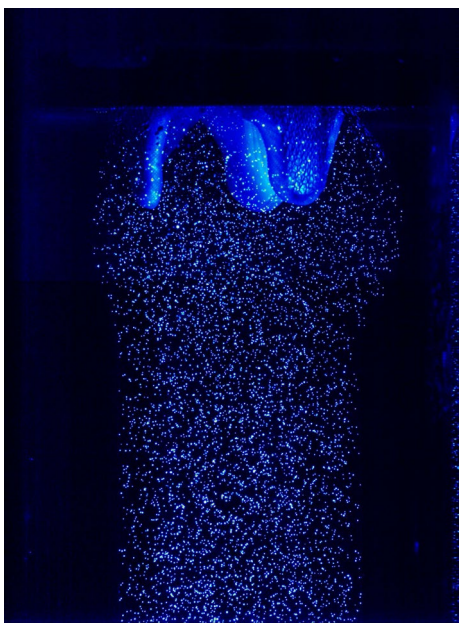

Fig. 6 Example of a recorded image of sparsely seeded flow for volume self-calibration. In the *upper part*, the frame of the heart valve prosthesis can be seen

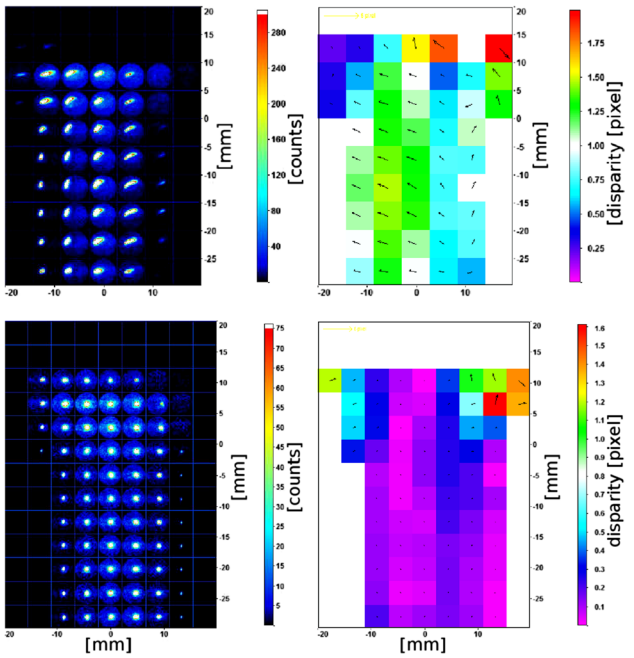

Fig. 7 Disparity maps (*left column*) and disparity vectors (*right column*) from first (*top row*) and last (*bottom row*) self-calibration run. The number of sub-volumes to collect disparities is increased during subsequent self-calibrations

views. This allowed to quantify the remaining distortion error by so-called disparity maps and disparity vectors which were then used to iteratively improve the camera calibration.

Figure 7 shows typical disparity maps and vectors resulting from volume self-calibration in the test cell. Four iterative applications of volume self-calibration were enough to reduce the disparities under 0.2 pixels in most parts of the measurement volume. In the Z-direction, two layers of 15 mm depth centered at $Z = \pm 7.5$ mm were used during all applications of volume self-calibration.

2.2.5 *Image processing*

Prior to tomographic reconstruction, the raw camera images were preprocessed: for background removal, a sliding minimum in a 5×5 pixel neighborhood was subtracted. Intensities were normalized with a local average to reduce inhomogeneities due to uneven laser illumination. Gaussian smoothing and subsequent sharpening was used to improve particle images. Finally, a masking technique was applied, such that only regions corresponding to the interior of the silicone phantom (flow region) would be considered for post-processing. The resulting measurement volume is indicated by the yellow shaded area in Fig. 5. It consists of a cylinder with a diameter of 24 mm and a height of 50 mm plus a part of the sinus portions defined by the inner

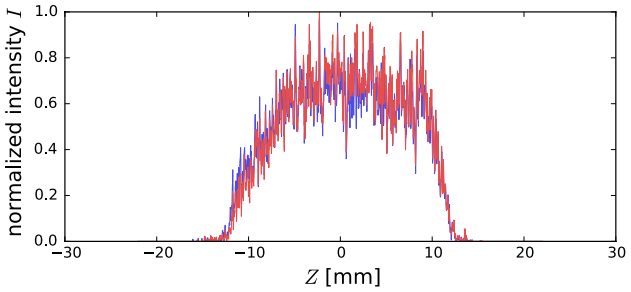

Fig. 8 Intensity-Z-profile from first (*blue*) and second (*red*) exposure. The measurement volume given by the phantom's inner geometry ranges from $Z = -12, \ldots, 12$ mm, disregarding the sinus portions

geometry of the silicone phantom and with a maximum radius of 17 mm. The upper border of the measurement volume reaches the tip of the frame of the bioprosthesis.

2.2.6 *Tomographic reconstruction*

Tomographic reconstruction was performed to generate a 3D voxel-based representation of the particle cloud in the measurement volume. To this end, we used a MLOS-MART algorithm: a multiplicative algebraic reconstruction technique [MART, see Herman and Lent (1976)] in combination with a one-pass MLOS (multiplicative line of sight) reconstruction to guess the initial intensity distribution [see Michaelis et al. (2010) for a comparison of different reconstruction algorithms used in tomographic PIV]. Seven MLOS-MART iterations were applied.

To assess the quality of the reconstruction, the cumulative intensity in planes with surface normals in Z-direction can be plotted against Z. This so-called intensity-Z-profile can show non-zero intensities outside the measurement volume (ghost intensity). Compared to the intensity inside the measurement volume, the ghost intensity should be small. Figure 8 shows a typical intensity Z-profile obtained during the experiments indicating only little ghost intensity close to the boundaries of the measurement volume.

2.2.7 *Particle image cross-correlation*

After tomographic reconstruction, a 3D cross-correlation was performed to determine the instantaneous 3D velocity field $\mathbf{U}(\mathbf{x}, t) = [U_x(\mathbf{x}, t), U_y(\mathbf{x}, t), U_z(\mathbf{x}, t)]^\mathsf{T}$, with $\mathbf{x} = [X, Y, Z]^\mathsf{T}$ within the whole measurement volume. We used Gaussian-shaped interrogation volumes and carried out two passes (predictor, corrector) for each of in total four steps. with interrogation sizes of $128 \times 128 \times 128$ voxels (one step) and $96 \times 96 \times 96$ voxels (three steps). Computational cost was reduced by volume binning with decreasing coarseness for each step. For all steps a 75 % overlap was chosen. Together with the image scale of 0.027 mm/

voxel this yielded a resolution for the vector field **U** of 0.0 27 × 96 × (1 − 0.75) ≈ 0.65 mm in all spatial directions. The total time for all post-processing steps to obtain a field with 67 × 76 × 67 velocity vectors was 22 min on a dual core 2.67 GHz Intel Xeon CPU with 144 GB of RAM.

2.3 Experimental protocol

Experiments were performed with constant flow rate and with pulsatile flow. For all experiments, a pulse separation of $\mathrm{d}t = 100\,\mu\mathrm{s}$ was chosen, resulting in an particle shift of 10 pixels for the highest expected velocities of 2.5–3.0 m/s.

2.3.1 Constant flow rate

For the constant flow measurements, the pump was operated such that the resulting flow rate was 13.5 l/min which corresponds to a mean velocity of $\bar{u} = 0.5\,\mathrm{m/s}$ in the nominal cross section of the measurement volume (bulk velocity), $\pi d_\mathrm{a}^2/4 = 452\,\mathrm{mm}^2$, where $d_\mathrm{a} = 24$ mm is the nominal inner diameter of the silicone phantom. The maximum effective stroke of the piston pump was $l_\mathrm{pp} = 0.12$ m with a diameter of $d_\mathrm{pp} = 0.1$ m. A constant piston velocity of $u_\mathrm{pp} = (d_\mathrm{a}/d_\mathrm{pp})^2\bar{u}$ was maintained during 4 s and image acquisition at 3.1 Hz was started after 2 s. In Fig. 9 the piston profile is shown together with seven image acquisition time points.

An ensemble average was calculated from the $M = 7$ instantaneous flow fields

$$\langle \mathbf{U}(\mathbf{x}) \rangle_M = \frac{1}{M} \sum_{k=1}^{M} \mathbf{U}(\mathbf{x}, t_k). \tag{1}$$

As a baseline, constant flow rate measurements without the aortic valve prosthesis were performed to identify non-valve-related flow structures.

2.3.2 Pulsatile flow

For pulsatile flow measurements, the pump was operated in a sinusoidal mode with a period of $T = 1$ s (60 beats per minute) according to

$$\bar{u}(t) = \bar{u}_\mathrm{max} \sin(2\pi t/T) \tag{2}$$

with the maximum bulk velocity $\bar{u}_\mathrm{max} = 0.5$ m/s. This value is motivated by the integral of Eq. (2) over the first half of the period, yielding a physiological stroke volume of 72 ml. In reality, the flow profile (over time) during systole is steeper and shorter than a sine and the maximum bulk velocities lie around 1 m/s (Schmidt and Thews 2007). The resulting flow rate through the test cell depended on opening and closure of the valves in the flow loop. It corresponded approximately to a cardiac output of 4.3 l/min.

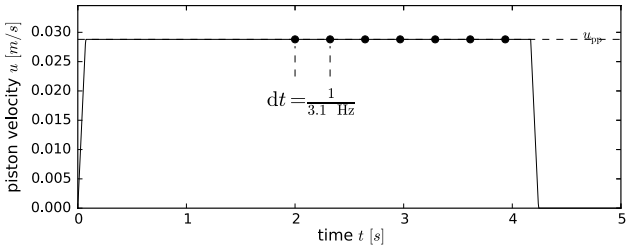

Fig. 9 Piston velocity profile (*solid line*) with acquisition times (*black dots*) for constant flow measurements

For the given Reynolds number $\mathrm{Re} = d_\mathrm{a}\bar{u}\mu/\rho = 1520$ and Womersley number $\alpha = d_\mathrm{a}\sqrt{2\pi\rho/(T\mu)} \approx 21$ flow instabilities were expected. Continuous acquisition of images yielded measurements of $\mathbf{U}(\mathbf{x}, t)$ at a temporal resolution of 3.1 Hz, limited by the frame rate of the camera.

Image acquisition was triggered at specific phases over a multitude of pulses. Because the flow in the test section nearly comes to rest during the diastole, the flow has essentially no memory of the preceding pulse. Therefore, we applied phase-averaging for different phases $\phi_j = j2\pi\,\mathrm{d}t/T$, with $j = 0, \ldots, 19$ and $\mathrm{d}t = 0.03$ s using $N = 10$ recordings each. This way we obtained a sequence of 20 phase-averaged flow fields

$$\langle \mathbf{U}(\mathbf{x}, t_j) \rangle_N = \frac{1}{N} \sum_{k=1}^{N} \mathbf{U}\big(\mathbf{x}, t_j + kT\big) \quad \text{with} \quad t_j = T\frac{\phi_j}{2\pi} \tag{3}$$

for a virtual frame rate of 33 Hz to resolve the first 0.57 s of a pulse. With this, a Reynolds decomposition of the instantaneous flow field can be considered

$$\mathbf{U} = \langle \mathbf{U} \rangle_N + \mathbf{u} \tag{4}$$

where **u** is the fluctuation of the velocity field. This allows to calculate the root-mean-square (rms) velocity fluctuation $u_\mathrm{rms} = \langle \mathbf{u} \cdot \mathbf{u} \rangle^{1/2}$ for each phase ϕ_j.

3 Results

In the following, we present the flow fields **U** and ⟨**U**⟩ resulting from the experiments with constant flow rate and with pulsatile flow through a 23 mm Carpentier–Edwards bioprosthetic valve. To produce Figs. 10, 11, 12, 13, 14 and 15 and the animation in the supplementary material we used the visualization software (Childs et al. 2012)

3.1 Constant flow rate

Figure 10 shows an instantaneous velocity field obtained for a constant flow rate . The resulting flow past the valve is highly unsteady due to flow instabilities (see Online

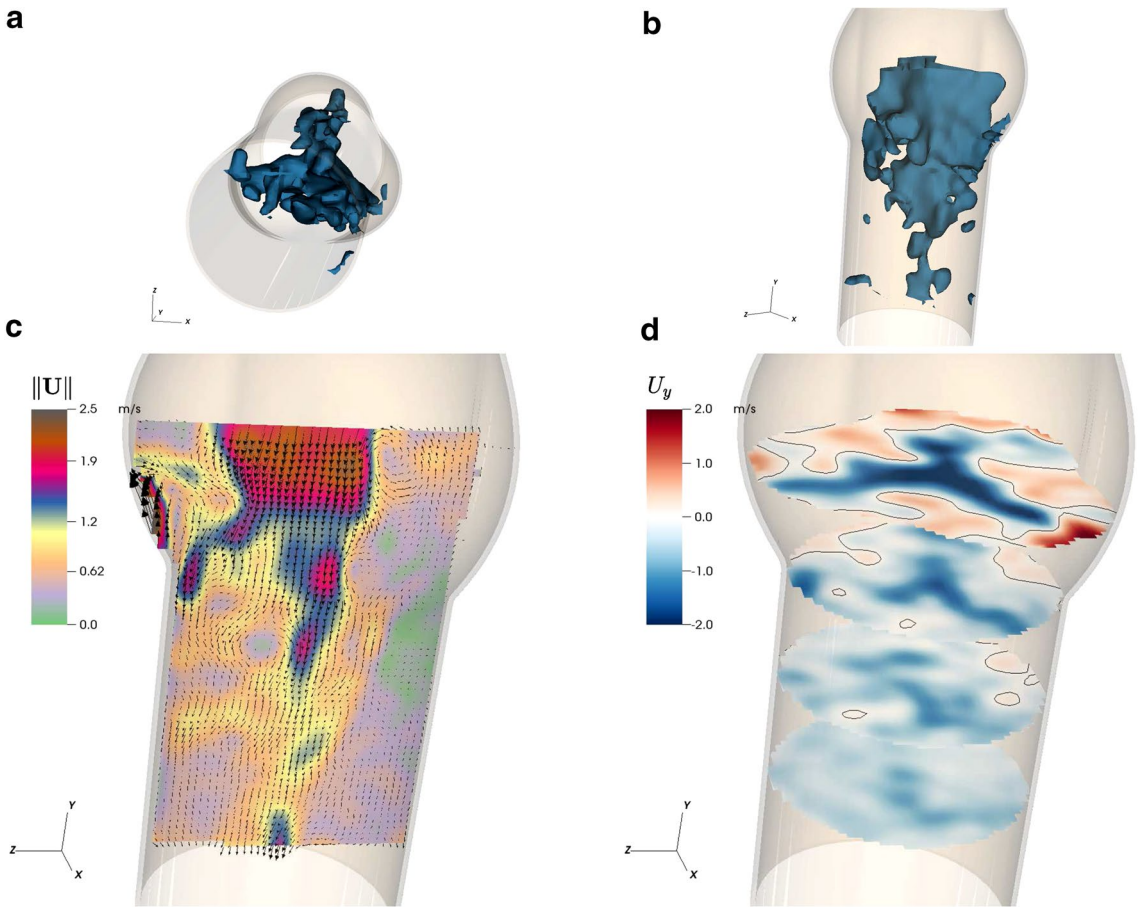

Fig. 10 Instantaneous flow field **U** in constant flow rate experiment: iso-surface of axial velocity $U_y = -1$ m/s (**a**, **b**); velocity field (*arrows*) and velocity magnitude $\|\mathbf{U}\|$ (*contour*) in the *YZ*-plane (**c**); U_y in cross sections at various distances from the valve, *solid line* indicates $U_y = 0$ m/s (**d**)

Resources *const_slice_x* and *const_slice_y*). Note that axial fluid flow through the valve during the systolic phase has a negative sign U_y due to the orientation of the world reference frame $\{X, Y, Z\}$.

We can find an axial jet along the centerline of the aortic root. Close to the aortic valve, the jet core is relatively narrow with high velocities (up to 2.1 m/s) and sharp shear layers. Further downstream, where the sinus portions lead into the straight tube (*sino-tubular junction*), the sharp velocity profile of the jet core rapidly dissipates to a smoother velocity profile with maximum velocities below 1 m/s. Cross-sectional slices through the flow field (Fig. 10d) show that this jet is not circular. However, the unsteady nature of the flow makes it difficult to identify detailed coherent flow structures.

Further inspection of the flow field shows that there are distinct regions of backflow and that the axial jet sheds small vortices in an irregular fashion (Fig. 10c).

Figure 11 shows the mean flow field for the constant flow rate experiment obtained by averaging over 7 instantaneous velocity fields. In contrast to the instantaneous flow field in Fig. 10, we can now clearly identify a star-like cross section of the central jet (Fig. 11a–c). This star-like shape is most expressed close to the sino-tubular junction of the aortic root where sharp shear layers separate this jet from regions of slow backflow. Note that the three tips of the star point into the sinus portions of the aortic root and *not* toward the *commissures* where the leaflets of native valves are attached to the aortic wall.

3.2 Pulsatile flow

Under pulsatile flow conditions, the unsteady phenomena make it increasingly difficult to interpret the flow field and it is meaningful to compute a phase-averaged mean flow field $\langle \mathbf{U} \rangle_N$ and velocity fluctuations as introduced in Eq. (4). Figures 12 and 13 show phase-averaged flow fields obtained during peak systole (at $t = 0.27$ s) and toward the end of the systolic phase (at $t = 0.36$ s), respectively. In the Online Resources *pulsatile_slice_x*, *pulsatile_slice_y* the complete movies obtained from phase-averaged flow fields in the period $0 \leq t \leq 0.57$ s are featured.

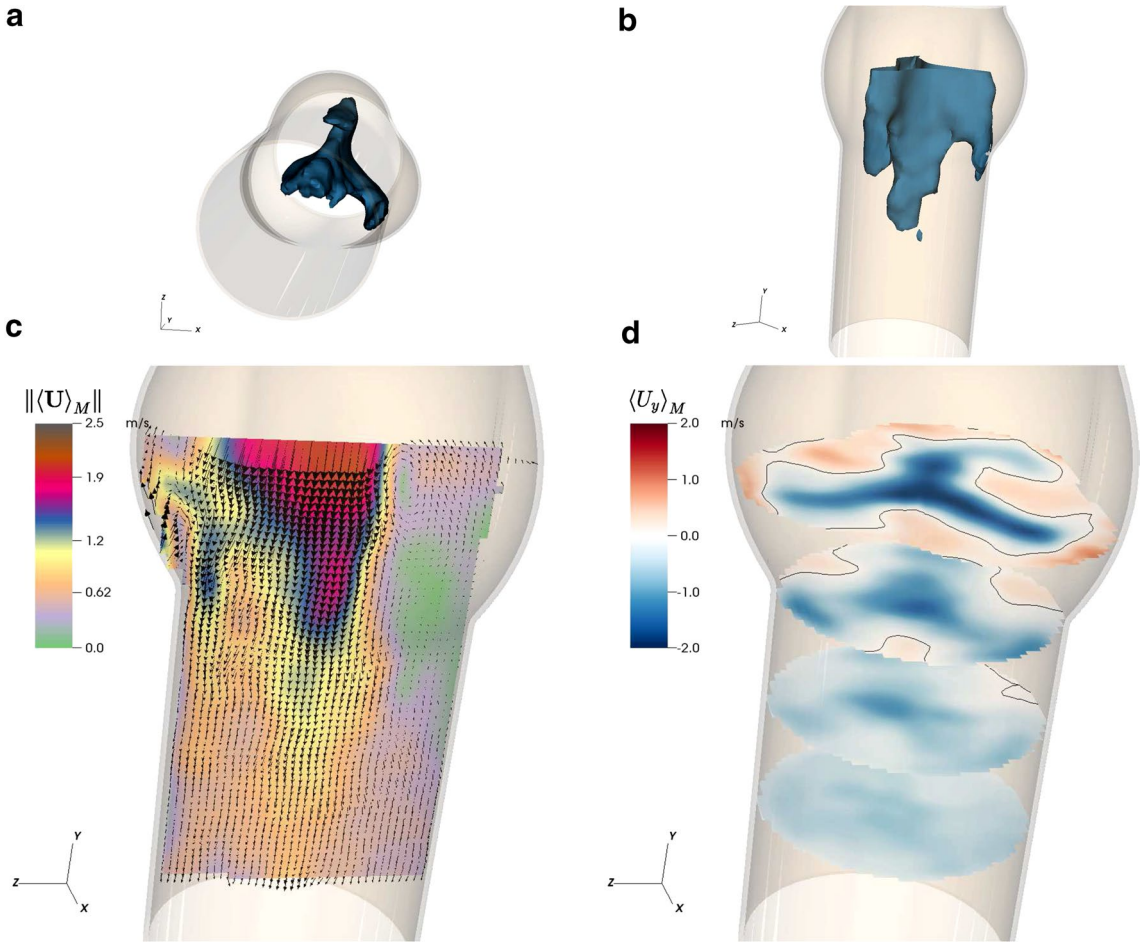

Fig. 11 Mean flow field $\langle \mathbf{U} \rangle_M$ in constant flow rate experiment: iso-surface of axial velocity $\langle U_y \rangle_M = -1\,\mathrm{m/s}$ (**a**, **b**); velocity field (*arrows*) and velocity magnitude $\|\langle \mathbf{U} \rangle_M\|$ (contour) in the *YZ*-plane (**c**); $\langle U_y \rangle_M$ in cross sections at various distances from the valve, *black line* indicates $\langle U_y \rangle_M = 0\,\mathrm{m/s}$ (**d**)

The flow field in the peak systolic phase (Fig. 12) resembles quite closely the mean flow field obtained in the constant flow rate experiment (see Fig. 11) featuring a star-like jet with three lobes pointing into the sinus portions. Between the lobes are three regions of backflow along the valve commissures (iso-surface for $\langle U_y \rangle_N = 0.3\,\mathrm{m/s}$ in Fig. 12). The star-like jet separates into a central jet core and three jet cores in the lobes with peak velocities slightly above 2 m/s. In the axial slice of Fig. 12c, we see the core of one of the lobes as well as the central jet core. Furthermore, the plot shows that the lobe cores impinge onto the vessel wall close to the sino-tubular junction. Finally, we can identify on the right side of the axial slice one of the regions of slow (<0.5 m/s) backflow toward the aortic valve. In Fig. 14, contour plots of the rms velocity fluctuation are presented. The strongest velocity fluctuations, $0.6 < u_{\mathrm{rms}} < 0.8\,\mathrm{m/s}$, appear in the shear layer between the central jet and the backflow regions. This can be explained by vortices which are generated in this region due to shear layer instabilities. Figure 15 shows vortices, visualized as λ_2-iso-surfaces, appearing in the shear layer around the central jet.

Toward the end of the systolic phase (Fig. 13), the fluid decelerates and only the central core of the star-like jet persists. Otherwise, the overall structure with a star-like jet and three regions of backflow remains intact until valve closure.

As a means of validation of the tomo-PIV measurements, we integrated the axial velocities over the cross section at the sino-tubular junction and compared the resulting flow rate to the flow rate generated by the piston pump. During the systolic phase, the unidirectional valve in the feedback tube is closed such that it can be expected that the two flow rates are the same. Figure 16 shows measured flow rates (ten per phase) together with the expected rates from the pump. Apart from some deviations at the beginning and end of the systolic phase, the measured flow rates agree fairly well with the pump profile. At $t = 0$ s the mean of the flow rate derived from tomo-PIV results is approximately

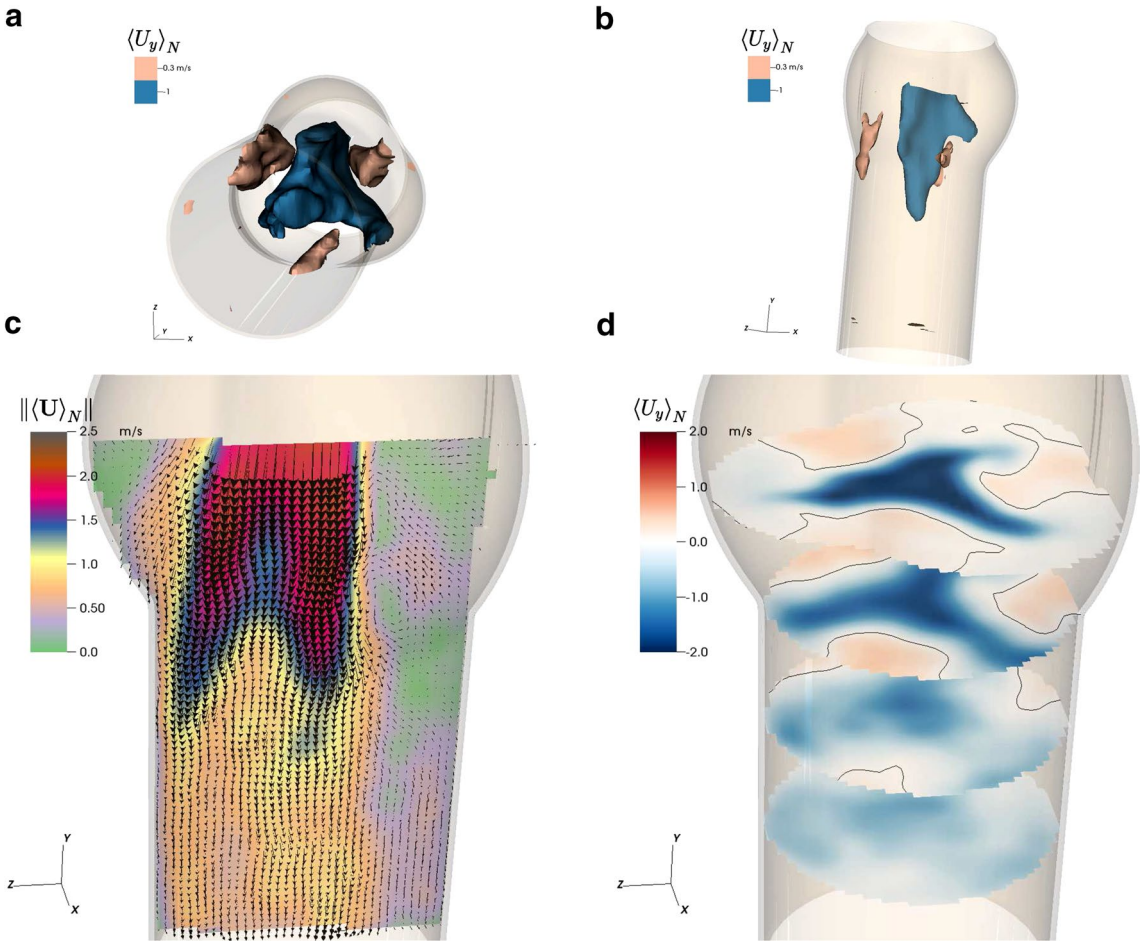

Fig. 12 Phase-averaged flow field $\langle \mathbf{U} \rangle_N$ in pulsatile flow experiment at $t = 0.27$ s (maximum systolic phase): iso-surface of positive and negative axial velocities $\langle U_y \rangle_N$ (**a**, **b**); velocity field (*arrows*) and velocity magnitude $\|\langle \mathbf{U} \rangle_N\|$ (contour) in the *YZ*-plane (**c**); $\langle U_y \rangle_N$ in cross sections at various distances from the valve, *solid line* indicates $\langle U_y \rangle_N = 0\,\mathrm{m/s}$ (**d**)

2.5 l/min, indicating that the valve is already open at this instant. Toward the end of the systolic phase, the aortic valve closes. At $t > 0.5$ s, the piston pump already induces a negative flow rate, giving rise to backflow through the valve (regurgitation) which persists until the valve is fully closed ($t > 0.6$ s). During and after valve closure, fluid is pumped through the feedback tube and therefore the piston profile is different than the measured flow rates.

4 Discussion

The measured flow fields for constant flow and for pulsatile flow provide good insight into the complex three-dimensional flow topology past a typical bioprosthetic heart valve. Comparison of the flow field during maximum systole with the flow field obtained for constant flow shows that both experimental configurations yield very similar results. This might not be the case anymore when the viscosity of the test fluid is adjusted to the viscosity of blood which yields higher Womersley numbers. Along with this observation, it should also be stated that the resulting flow was highly unsteady due to flow instabilities (for both experimental protocols) such that the results had to be suitably averaged. It is to be expected that this unsteady nature of the flow will be even more expressed when using a fluid with a viscosity similar to the one of blood, leading to higher Reynolds numbers.

Under pulsatile conditions, the tomo-PIV experiments presented here were conducted with an acquisition frequency of the same order as the frequency of the pulsatile flow. Phase-averaging for different instances of the systolic phase revealed the dynamic behavior of the mean flow. To reveal the full dynamic behavior of the instantaneous velocity field, time-resolved tomo-PIV experiments with higher acquisition frequency have to be performed.

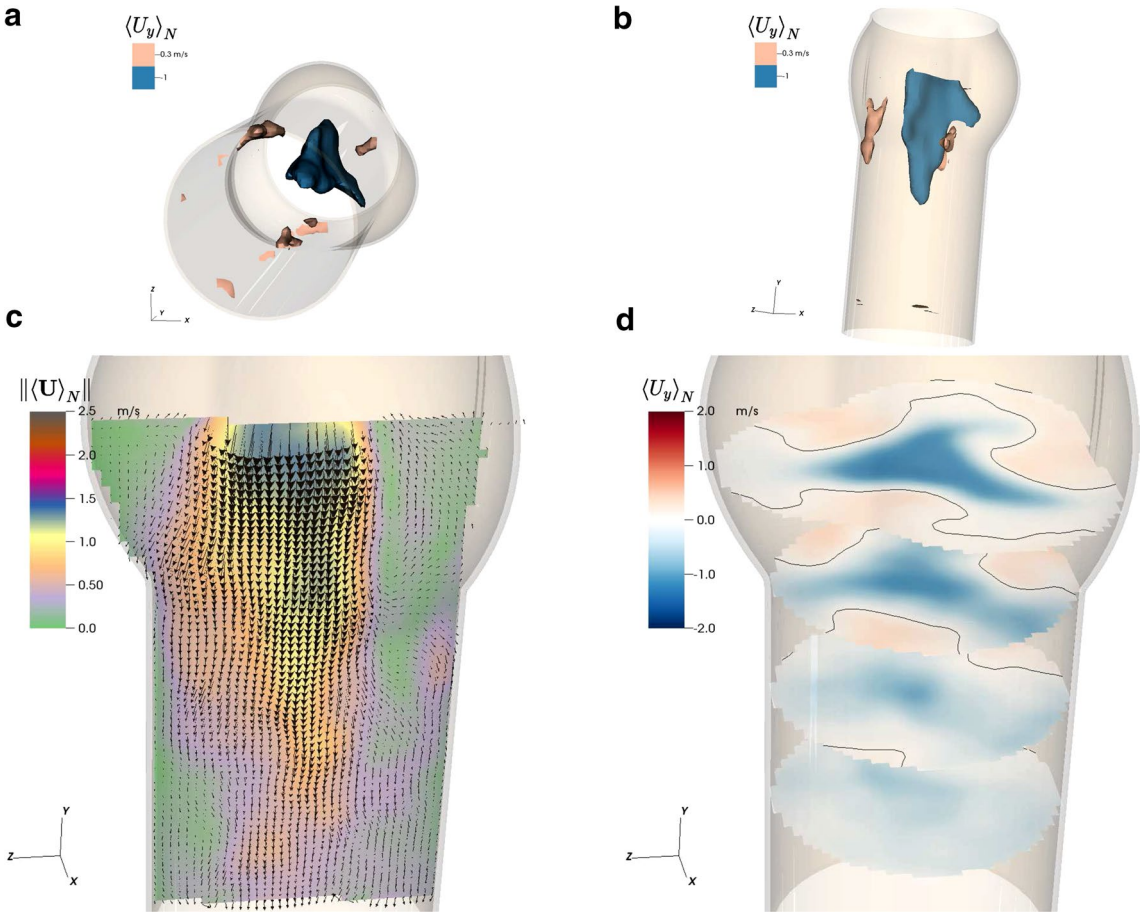

Fig. 13 Phase-averaged flow field $\langle \mathbf{U} \rangle_N$ in pulsatile flow experiment at $t = 0.36$ s (end systolic phase): iso-surface of positive and negative axial velocities $\langle U_y \rangle_N$ (**a**, **b**); velocity field (*arrows*) and velocity magnitude $\|\langle \mathbf{U} \rangle_N\|$ (contour) in the *YZ*-plane (**c**); $\langle U_y \rangle_N$ in cross sections at various distances from the valve, *solid line* indicates $\langle U_y \rangle_N = 0$ m/s (**d**)

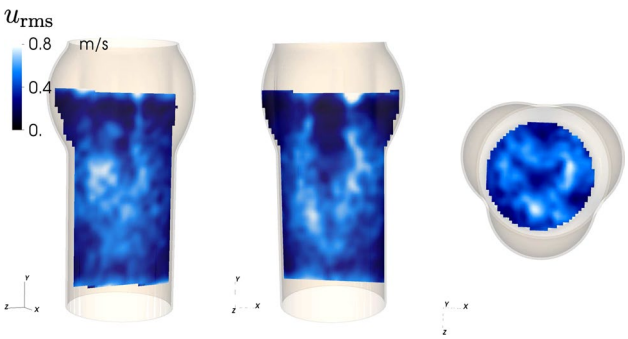

Fig. 14 Contour plot of the rms velocity fluctuation u_{rms} corresponding to the phase-averaged flow field in Fig. 12. From *left* to *right*: *YZ*-plane, *XY*-plane and *XZ*-plane

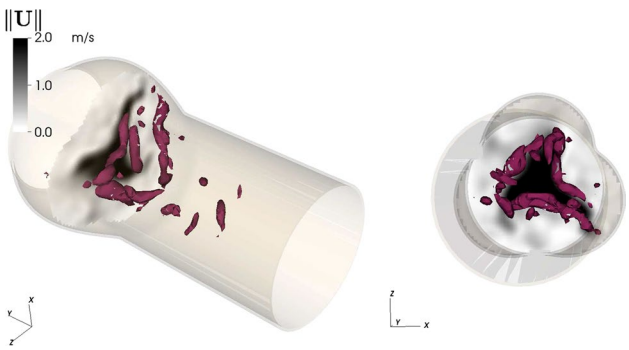

Fig. 15 Iso-surfaces for $\lambda_2 = -0.0025$ at $t = 0.27$ s. Contour plot on cross-sectional slice indicates magnitude of the instantaneous flow field

4.1 Star-like jet

The most prominent feature of the resulting flow fields is the star-like jet and the three regions of backflow (e.g., Fig. 12b). A star-like flow profile has been reported before for a different valve type (Leo et al. 2006); however, the three lobes of this star pointed toward the commissures.

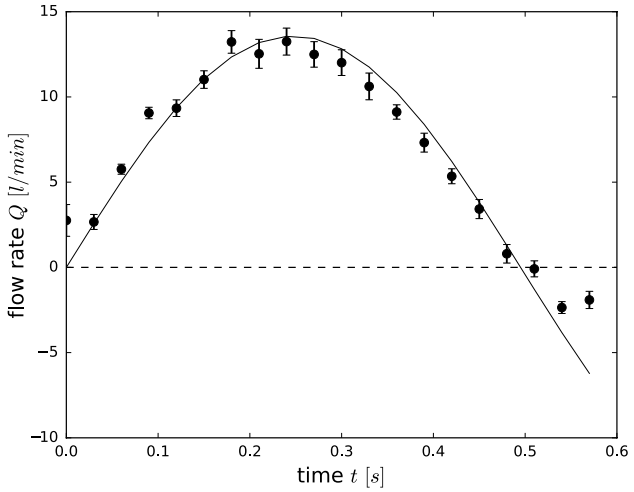

Fig. 16 Measured flow rates mean (*black dots*) and standard deviation (*bars*) and displacement volume rate of the pump (*line*)

Therefore, the present start like jet is rotated by 60° with respect to the jet reported by Leo et al. (2006). We attribute this difference to the particular shape of the valve orifice which influences flow structures past the heart valve. The shape of the valve orifice in the systolic phase is a result of the leaflet kinematics. In the studied valve, the leaflets are tightly fixed to the valve struts and expand into the sinus portions during systole. The shape of the open orifice is not round but triangular with a tip in each sinus portion. As a consequence, high momentum fluid impinges on the vessel wall in three different regions. Therefore, the lobes of the star-like jet induce high local wall shear stresses.

4.2 Recirculation and vortical flow

The results also show large recirculation zones associated with the three lobes of the star-like jet. The zones extend past the sino-tubular junction (see negative velocity iso-surfaces in Fig. 12a, b).

Traditionally, vortices are assumed more upstream. According to an early study by Bellhouse and Talbot (1969), vortices in the sinus portions, induced during systole, play a major role in the self-regulation of the valve closing mechanism: the pressure distribution in the sinus portions is affected by these vortices in a way that the leaflet position is stabilized, and a smooth closure is initiated relatively early, minimizing regurgitation. The presented results do not show any distinct vortices in the sinus portions. Firstly, these regions are not fully covered by the measurement volume and secondly the valve is yet positioned relatively far above the sinus portions, due to the design of the mount.

4.3 Limitations

As already indicated previously, the principal limitation of the present experimental setup is the frame rate of the cameras. The fastest flow structures in the flow past a heart valve are probably the vortices which are shed from undulating leaflets. From the separation of vortices (Fig. 10c), it can be estimated that the shedding frequency is in the order of 100 Hz. Hence, the acquisition rate necessary to measure the flow field past a heart valve in a fully time-resolved manner may be as high as 200 Hz.

Furthermore, the measurements presented here have a limited precision in the near wall regions. The chosen interrogation window size is suitable for measurements in the bulk, where moderate velocity gradients occur, but it does not satisfy the conditions to measure thin boundary layers. For this purpose, a smaller interrogation window size, e.g., $32 \times 32 \times 32$ voxels together with a much higher seeding density would be needed. Therefore, we are not presenting any results or conclusions on the near wall velocity fields.

Even though there is essentially no compliance in the system, we have observed a positive phase shift between pressure and piston velocity, which potentially affects the opening and closing of the valves and can influence the flow profile especially near beginning and near end of systole. This can be explained by the inertia of the fluid in the feedback tube which can cause a negative pressure gradient across the valve, even if the piston has zero velocity. Improving the flow loop design by adding, for instance, a compliance chamber is expected to mitigate this problem.

5 Concluding remarks

In this study, a new concept of applying tomo-PIV to internal flows in general is demonstrated and results of the pulsatile mean flow field past a heart valve are presented. The study clearly illustrates the potential of tomo-PIV in helping characterizing biological flows and points out current limitations of the presented setup.

Tomo-PIV is a powerful new method for studying the flow past bioprosthetic heart valves. Distinct flow features like the three-lobe topology of the instantaneous flow field can be detected and further analyzed. This way, the most pronounced asymmetries in the flow profile, containing high wall shear stresses on one side and recirculation and internal shear layers on the other side, can be accurately localized and appreciated in the context of a complex three-dimensional flow topology.

References

Amatya D, Troolin RD, Longmire EK (2009) 3D3C Velocity measurements downstream of artificial heart valves. In: 8th International Symposium on Particle Image Velocimetry

Atkinson C, Coudert S, Foucaut JM, Stanislas M, Soria J (2010) The accuracy of tomographic particle image velocimetry for measurements of a turbulent boundary layer. Exp Fluids 50:1031–1056

Bellhouse BJ, Talbot L (1969) Fluid mechanics of the aortic valve. Br Heart J 31(3):391

Bellofiore A, Quinlan NJ (2011) High-resolution measurement of the unsteady velocity field to evaluate blood damage induced by a mechanical heart valve. Ann Biomed Eng 39:2417–29

Blake JR, Easson WJ, Hoskins PR (2009) A dual-phantom system for validation of velocity measurements in stenosis models under steady flow. Ultrasound Med Biol 35:1510–1524

Borazjani I (2013) Fluid–structure interaction, immersed boundary-finite element method simulations of bio-prosthetic heart valves. Comput Methods Appl Mech Eng 257:103–116

Borazjani I, Ge L, Sotiropoulos F (2010) High-resolution fluid–structure interaction simulations of flow through a bi-leaflet mechanical heart valve in an anatomic aorta. Ann Biomed Eng 38:326–344

Brücker C, Steinseifer U, Schröder W, Reul H (2002) Unsteady flow through a new mechanical heart valve prosthesis analysed by digital particle image velocimetry. Meas Sci Technol 13:1043–1049

Buchmann NA, Atkinson C, Jeremy MC, Soria J (2011) Tomographic particle image velocimetry investigation of the flow in a modeled human carotid artery bifurcation. Exp Fluids 50:1131–1151

Childs H, Brugger E, Whitlock B, Meredith J, Ahern S, Pugmire D, Biagas K, Miller M, Harrison C, Weber GH, Krishnan H, Fogal T, Sanderson A, Garth C, Bethel EW, Camp D, Rübel O, Durant M, Favre JM, Navrátil P (2012) An End-User Tool For Visualizing and Analyzing Very Large Data. In: Bethel EW, Childs H, Hansen C (eds) High Performance Visualization-Enabling Extreme-Scale Scientific Insight. CRC Press, New York, pp 357–372

Dasi LP, Ge L, Simon AH, Sotiropoulos F, Yoganathan PA (2007) Vorticity dynamics of a bileaflet mechanical heart valve in an axisymmetric aorta. Phys Fluids 19:6

De Tullio MD, Cristallo A, Balaras E, Verzicco R (2009) Direct numerical simulation of the pulsatile flow through an aortic bileaflet mechanical heart valve. J Fluid Mech 622:259

Elsinga GE, Marusic I (2010) Evolution and lifetimes of flow topology in a turbulent boundary layer. Phys Fluids 22:1

Elsinga GE, Wieneke B, Scarano F, van Oudheusden BW (2005) Assessment of Tomo-PIV for three-dimensional flows. In: 6th International Symposium on Particle Image Velocimetry, pp 1–10

Elsinga GE, Scarano F, Wieneke B, Oudheusden BW (2006) Tomographic particle image velocimetry. Exp Fluids 41:933–947

Ge L, Jones SC, Sotiropoulos F, Healy TM, Yoganathan AP (2003) Numerical simulation of flow in mechanical heart valves: grid resolution and the assumption of flow symmetry. J Biomech Eng 125:709–718

Ge L, Leo HL, Sotiropoulos F, Yoganathan AP (2005) Flow in a mechanical bileaflet heart valve at laminar and near-peak systole flow rates: CFD simulations and experiments. J Biomech Eng 127:782–797

Geoghegan PH, Na Buchmann, Spence CJT, Moore S, Jermy M (2012) Fabrication of rigid and flexible refractive-index-matched flow phantoms for flow visualisation and optical flow measurements. Exp Fluids 52(5):1331–1347

Griffith BE (2012) Immersed boundary model of aortic heart valve dynamics with physiological driving and loading conditions. Int J Numer Methods Biomed Eng 28:317–345

Hegner F, Hess D, Ch B (2015) Volumetric 3D PIV in heart valve flow. In: 11th International Symposium on Particle Image Velocimetry

Herman GT, Lent A (1976) Iterative reconstruction algorithms. Comput Biol Med 6:273–294

Jamieson WR, Janusz MT, Burr LH, Ling H, Miyagishima RT, Germann E (2001) Carpentier–Edwards supraannular porcine bioprosthesis: second-generation prosthesis in aortic valve replacement. Ann Thorac Surg 71:S224–S227

Kaminsky R, Kallweit S, Weber HJ, Claessens T, Jozwik K, Verdonck P (2007) Flow visualization through two types of aortic prosthetic heart valves using stereoscopic high-speed particle image velocimetry. Artif Organs 31:869–879

Leo HL, Dasi LP, Carberry J, Simon HA, Yoganathan AP (2006) Fluid dynamic assessment of three polymeric heart valves using particle image velocimetry. Ann Biomed Eng 34:936–952

Manning KB, Kini V, Fontaine AA, Deutsch S, Tarbell JM (2003) Regurgitant flow field characteristics of the St. Jude bileaflet mechanical heart valve under physiologic pulsatile flow using particle image velocimetry. Artif Organs 27:840–846

Markl M, Harloff A, Bley TA, Zaitsev M, Jung B, Weigang E, Langer M, Hennig J, Frydrychowicz A (2007) Time-resolved 3D MR velocity mapping at 3T: improved navigator-gated assessment of vascular anatomy and blood flow. J Magn Reson Imaging 25:824–831

Markl M, Kilner PJ, Ebbers T (2011) Comprehensive 4D velocity mapping of the heart and great vessels by cardiovascular magnetic resonance. J Cardiovasc Magn Reson 13:7

Michaelis D, Novara M, Scarano F, Wieneke B (2010) Comparison of volume reconstruction techniques at different particle densities. In: 15th International Symposium on Applications of Laser Techniques to Fluid Mechanics, Lisbon, Portugal

Raffel M, Willert CE, Wereley ST, Kompenhans J (2007) Particle image velocimetry: a practical guide, 2nd edn. Springer, Berlin, Heidelberg

Scarano F (2012) Tomographic PIV: principles and practice. Meas Sci Technol 24(012):001

Scarano F, Poelma C (2009) Three-dimensional vorticity patterns of cylinder wakes. Exp Fluids 47:69–83

Schmid PJ, Violato D, Scarano F (2012) Decomposition of time-resolved tomographic PIV. Exp Fluids 52:1567–1579

Schmidt RF, Thews G (2007) Physiologie des Menschen, 30. Auflage. Springer, Berlin, Heidelberg

Schröder A, Geisler R, Elsinga GE, Scarano F, Dierksheide U (2008) Investigation of a turbulent spot and a tripped turbulent boundary layer flow using time-resolved tomographic PIV. Exp Fluids 44:305–316

Schröder A, Geisler R, Staack K, Elsinga GE, Scarano F, Wieneke B, Henning A, Poelma C, Westerweel J (2011) Eulerian and Lagrangian views of a turbulent boundary layer flow using time-resolved tomographic PIV. Exp Fluids 50:1071–1091

Stergiopulos N, Westerhof BE, Westerhof N (1999) Total arterial inertance as the fourth element of the windkessel model. Am J Physiol 276:H81–H88

Swanson WM, Clark RE (1974) Dimensions and geometric relationships of the human aortic value as a function of pressure. Circ Res 35(6):871–882

Violato D, Scarano F (2011) Three-dimensional evolution of flow structures in transitional circular and chevron jets. Phys Fluids 23:12

Wieneke B (2008) Volume self-calibration for 3D particle image velocimetry. Exp Fluids 45:549–556

Yousif MY, Holdsworth DW, Poepping TL (2010) A blood-mimicking fluid for particle image velocimetry with silicone vascular models. Exp Fluids 50(3):769–774